Systematic structural study in praseodymium compressed in a neon pressure medium up to 185 GPa

E. F. O'Bannon III,[1,*] O. S. Pardo,[2] P. Söderlind,[1] D. Sneed,[1] M. J. Lipp,[1] C. Park,[3] and Zs. Jenei[1]

[1]*Physics Division, Physical & Life Sciences Directorate, Lawrence Livermore National Laboratory, Livermore, California 94550, USA*

[2]*Seismological Laboratory, California Institute of Technology, Pasadena, California 91125, USA*

[3]*High Pressure Collaborative Access Team, X-Ray Science Division, Argonne National Laboratory, Argonne, Illinois 60439, USA*

(Received 24 January 2022; revised 18 March 2022; accepted 5 April 2022; published 25 April 2022)

Angle-dispersive x-ray powder diffraction experiments have been performed on praseodymium metal compressed in a soft pressure-transmitting medium at ambient temperature up to 185 GPa. We observe the previously reported high-pressure structural transition sequence up to 20 GPa and the coexistence of body-centered orthorhombic (bco) Pr and α-U Pr from ~20 up to ~38 GPa. The α-U structure of Pr is stable from 20 to 185 GPa, and no evidence of the proposed transition to a primitive orthorhombic phase >147 GPa was observed. With density functional theory (DFT), we calculated the lattice parameters and y coordinate for α-U Pr and found good agreement between our calculations and experimental measurements. The obtained DFT energies of the proposed primitive orthorhombic ($P2_12_12_1$) and the α-uranium phases at ~150 GPa show that the α-uranium phase is lower in energy. Hence, neither our experimental data nor our DFT results support the transition to a primitive orthorhombic phase >150 GPa. DFT suggests, however, that Pr may transform to the $P2_12_12_1$ phase above ~220 GPa. We also compare the axial ratios and lattice parameters of praseodymium to α-uranium structured Nd, Ce, and U.

DOI: 10.1103/PhysRevB.105.144107

I. INTRODUCTION

At ambient conditions, $4f$ electrons in lanthanides are localized, i.e., they occupy states that are essentially atomic with little hybridization with each other. Under strong compression, the nature of these electrons changes; as atoms approach each other, eventually, the $4f$ states hybridize and become more metallic or bandlike. The fundamental problem in describing this transition, from localized to delocalized or itinerant electrons, has not been solved and remains one of the great challenges for condensed matter theory. Theoretical frameworks exist to deal with either extreme: strong electron correlation with a Hubbard U and large intra-atomic Coulomb repulsion for the localized state and density functional theory (DFT) for the delocalized state.

The high-pressure behavior of lanthanides has been extensively studied experimentally, and these studies have contributed to our understanding of f-electron systems at high densities [1–6]. A common phase-transition sequence has been described in the lanthanides La through Lu [6] (notable exceptions are Ce, Eu, and Yb). Recently, McMahon *et al.* [1] showed that the long accepted monoclinic structure ($mC4$) of the collapsed high-pressure phase reported in Nd, Tb, Gd, Dy, Ho, Er, and (probably) Tm is incorrect. The collapsed phase in Nd is an 8-atom orthorhombic structure ($oF8$), while the collapsed phase for the rest of them is a 16-atom orthorhombic structure ($oF16$) [1]. This is still an incredibly active area of research where studies in the last two years have expanded the pressure range over which Sm to 222 GPa [7], Nd to 302 GPa [8], and Ho to 282 GPa [9] have been investigated. The previously reported volume-collapse transition in solid Gd has also been recently reinvestigated and has been found not to occur [10].

Most of the high-pressure work on lanthanides has been performed using no pressure-transmitting medium (PTM) [7–9,11–14]. It is commonly stated that lanthanides are extremely soft materials, and they are highly reactive, so reactivity between the sample and the pressure medium is often cited as a concern. However, the importance of hydrostaticity is widely recognized by the high-pressure community. Takemura [15] outlines how nonhydrostatic stress can affect phase transitions such as lowering the onset pressure of a phase transition, stabilizing different crystalline phases, and even inducing amorphization. Moreover, it is known that equation of state (EOS) parameters derived from nonhydrostatic measurements are biased [16,17]. It is possible that, at lower pressures, the influence of nonhydrostatic conditions is minimal in soft materials such as lanthanides. Most likely, nonhydrostatic conditions play an important role at pressures exceeding 100 GPa.

Pr is somewhat unique among the other lanthanides. At lower pressure, it follows the established phase-transition sequence, and it crystallizes into the double hexagonal close-packed (dhcp) structure at ambient conditions [$P6_3/mmc$ and $hP4$]. Above ~3–4 GPa, it transforms to a face-centered cubic (fcc) structure [$Fm\bar{3}m$ and $cF4$] and, above ~7–8 GPa, to a distorted-fcc (d-fcc) structure [$R\bar{3}m$ and $hR24$] [13,18–21]. However, above ~13 GPa, a body-centered orthorhombic (bco) phase or slight distortion thereof is observed [21] which deviates from the established phase-transition sequence seen in the other lanthanides. Above ~20 GPa, Pr transforms

*obannon2@llnl.gov

to its collapsed phase which is α-uranium (α-U) structured [*Cmcm* and *oC*4]. This is different than the collapsed phase of other lanthanides Nd, Tb, Gd, Dy, Ho, Er, and (probably) Tm that has recently been reported [1]. Interestingly, while many studies have reported the *P*-*V* curve of the α-uranium phase of Pr, reports of the lattice parameters across the entire pressure range of their measurements are lacking [13,18–23]. Therefore, the behavior of the unit cell under compression is unknown, unlike U, where this has been well characterized up to 100 GPa [24,25]. Velisavljevic *et al.* [12] report electrical resistivity measurements on Pr up to 179 GPa and note that there is a plateau observed in the electrical resistance >150 GPa. Velisavljevic and Vohra [13] investigated Pr using x-ray diffraction techniques and report a transition to a primitive orthorhombic structure at ∼147 GPa (space group $P2_12_12_1$), citing their previous electrical resistance work as further evidence to support this phase transition. Based on the phase-transition sequences, we may expect to see this transition in Nd. However, Nd has recently been reinvestigated, and the α-uranium structure is observed to be stable from ∼100 to 302 GPa with no evidence of a transition to the primitive orthorhombic structure. This so-called post-α-uranium structure has not been observed in any other lanthanides to date.

Here, we describe diffraction studies on Pr compressed in a Ne PTM up to a maximum pressure of 185 GPa. These were performed to (i) investigate the post-α-uranium phase transition reported by Ref. [13], (ii) characterize the lattice parameters and the *y* coordinate across a wide pressure range, and (iii) compare these results with other elements which adopt the α-uranium structure. Since we are focusing on the high-pressure behavior of praseodymium in this paper, the best starting point for theory is DFT. Previous DFT modeling was able to reproduce the α-uranium phase satisfactorily [26]. For this phase, the present results are very similar to the previous calculations. However, the proposed primitive orthorhombic phase ($P2_12_12_1$) has not been modeled to date. As before, electron correlations are dealt with in relativistic DFT that includes spin-orbit interaction and a self-consistent scheme to address orbital-orbital interactions, or orbital polarization (OP). Here, we have investigated praseodymium in the α-uranium phase as well as the proposed $P2_12_12_1$ phase across a wide pressure range from 20 up to ∼300 GPa using DFT + OP.

II. METHODS

A. Experimental

Two experimental runs were carried out using membrane diamond anvil cells (DACs) [27] which were equipped with 500 μm flat diamond anvils for measurements <25 GPa and 300/100 μm beveled diamond anvils for measurements >100 GPa. For the low-pressure run, a stainless-steel gasket was pre-indented to ∼50 μm, and a 200 μm hole was drilled with an electric discharge machine (run 1). For the high-pressure run, a Re gasket was used, and it was pre-indented to ∼20 μm, and a 40 μm hole was drilled using a laser milling machine (run 2). We obtained a Pr foil sample from Alfa-Asear with a purity of 99.5%. We measured the ambient sample and obtained the following lattice parameters from our Rietveld refinement using a $P6_3/mmc$ space group [28]; $a = 3.6763(15)$ Å and $c = 11.8612(28)$ Å which are in good agreement with previous studies [19,20]. Here, 99.9% pure Cu spheres obtained from Alfa-Asear were used as the pressure marker for both runs using the reported EOS from Ref. [29]. Ne was also used to estimate the pressure using the EOS reported in Ref. [30]. For both high-pressure runs, a Cu sphere 3–6 μm in diameter and a ruby sphere ∼3 μm in diameter were loaded into the sample compartment. A small piece of Pr was cut off the main Pr foil sample and loaded into the sample compartment in a glovebox with a dry nitrogen environment to prevent oxidation of the sample. The DACs were closed in the glovebox to prevent oxidation of the sample before gas loading. We loaded 99.999% pure Ne obtained from Linde as the PTM in our high-pressure gas loader at a pressure of 1.8 kbar and used ruby luminescence to set the initial pressure of each cell using the ruby calibration reported in Ref. [31].

Angle-dispersive x-ray diffraction experiments were carried out at the High-Pressure Collaboration Access Team (HPCAT) at beamline 16 BMD. A monochromatic x-ray beam of ∼25 keV ($\lambda = 0.4959$ Å) was focused to a beam size of $\sim 4 \times 7\ \mu m^2$. Diffraction patterns were collected with a MAR-345 image plate detector with exposure times up to 300 s. Sample positioning and centering was accomplished by the fly scan method [32], and detector distance and orientation were calibrated using a CeO_2 standard. Initial x-ray diffraction grid scans of both sample compartments revealed low intensity single-crystal like peaks in both samples which belong to a cubic contaminant.

The two-dimensional diffraction patterns were radially integrated using DIOPTAS [33] to obtain an intensity curve of the diffraction peaks as a function of the 2θ angle, which were analyzed to obtain peak positions using our in-house analysis codes in the ORIGINPRO software package. Pr volumes were calculated directly from fitted peak positions and compared with full-profile Rietveld refinements at various pressures using GSAS-II [34]. The pressure inside the high-pressure chamber of the DACs was estimated by measuring the unit cell volume of Cu and Ne using the (111) reflection and the EOSs reported by Refs. [29,30]. The lattice parameters for Cu, Ne, and Pr from both runs calculated directly from fitted peak positions and the pressure estimation from Cu and Ne are tabulated in Ref. [28].

Rietveld refinements for α-U Pr were carried out in GSAS-II [34] beginning at ∼20 GPa after background removal and instrument parameter calibration. Starting lattice parameters values for the 20 GPa pattern were taken from Evans *et al.* [21]. Pr-VII was present in patterns up to ∼38 GPa, and this phase was fit using Pawley refinement. Four atoms within α-U Pr occupy the 4*c* Wyckoff positions at $(0, y, \frac{1}{4})$, $(0, -y, \frac{3}{4})$, $(\frac{1}{2}, \frac{1}{2}+y, \frac{1}{4})$, and $(\frac{1}{2}, \frac{1}{2}-y, \frac{3}{4})$, and an initial *y* coordinate of 0.1 was chosen following Velisavljevic and Vohra [13]. We tested three types of Rietveld fits that included fitting the pattern with and without preferred orientation and/or microstrain within the sample. The data presented here are the results of fitting the patterns with preferred orientation and microstrain, as without these parameters, the instrument profile and atomic positions alone cannot account for relative peak intensity with increasing pressure. The fitting procedure varied the lattice

parameters first, then iterated between varying the preferred orientation and microstrain model, and finally, the y coordinate was fit last for all pressures. The refined values of the patterns were taken to be the initial values of the subsequent pattern. Lattice parameters of Ne, Cu, and α-U Pr as well as R_{wp} from our fits and the refined y coordinate obtained from our Rietveld refinements are shown in Ref. [28].

B. Theoretical

We expect DFT to be relevant for high-pressure praseodymium, but we have further improved upon the model to better handle the localized $4f$ states at ambient conditions by an extension that couples the magnetic orbital moments with each other. This OP phenomenon is related to Hund's second rule for the atoms and attempts to bring some atomic physics into the DFT model. It has been shown that DFT + OP can relatively accurately reproduce known bonding properties such as lattice constants and bulk moduli as well as magnetic properties for the rare-earth metals [35].

For high-pressure conditions, where one certainly expects delocalization of the $4f$ electrons, DFT + OP is a sensible approach to study EOS and crystal-structure stability. We employ an all-electron full-potential linear muffin-tin orbital method [36] that includes spin-orbit coupling and assumes the generalized gradient approximation (GGA) [37] for the electron exchange and correlation functional. Two very important aspects of this methodology are that, first, no geometrical approximations are adopted (important for distorted crystal structures), and second, no pseudopotential approximation for core electrons is assumed (important for highly compressed materials).

Details of the calculations are like those we have done previously for the rare-earth metals [35] that also show GGA is superior to the local density approximation for praseodymium. Briefly, the setup includes $5s$, $5p$, $6s$, $6p$, $5d$, and $4f$ states that have two energy parameters associated with them for a so-called double basis set. Spin-orbit coupling and OP are included for the d and f states only, and the overall computational scheme is entirely free from adjustable parameters. The crystal structures we calculate have various numbers of atoms, but generally, for a 1-atom structure, we use ~500 k points in the irreducible Brillouin zone and correspondingly less for multi-atom phases. This choice safely converges the total energies. Our calculated lattice parameters and y coordinate for α-U Pr are shown in Ref. [28].

III. RESULTS AND DISCUSSION

Diffraction patterns were collected in run 1 up to a maximum pressure of 22.4 GPa in a Ne PTM, and these data confirm the phase-transition sequence that has been previously reported [18,19,21]. Figure 1 shows integrated diffraction patterns from each phase in the structural sequence up to the collapsed α-U phase. In all the patterns collected in run 1, we observe low-intensity reflections consistent with one cubic contaminant (fcc structure), most likely one of the same contaminants reported by Evans *et al.* [21]. An example diffraction pattern and the lattice parameter of this contaminant as a function of pressure are shown in the Supplemental

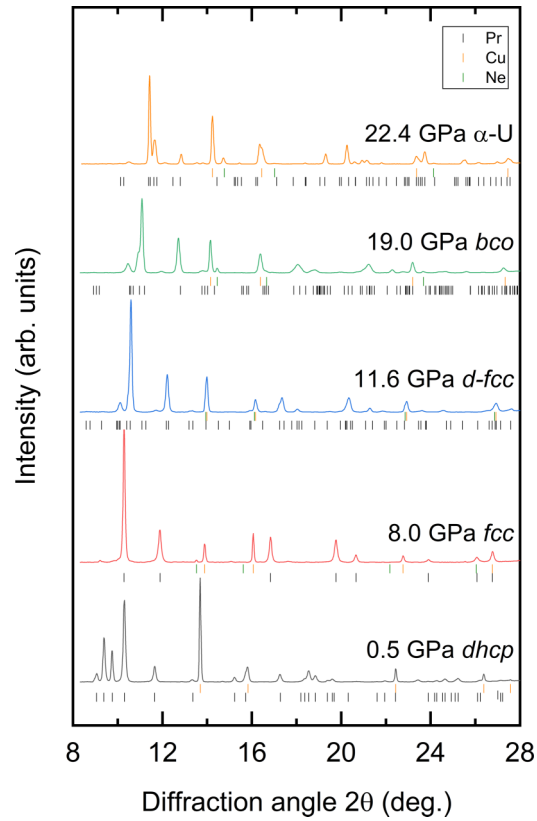

FIG. 1. Integrated diffraction patterns collected from Pr on run 1 during pressure increase to 22.4 GPa collected at 16 BMD at the Advanced Photon Source using a wavelength of $\lambda = 0.4959$ Å. Tick marks below each pattern mark Pr, Cu, and Ne. All patterns are single phase except the 8.0 GPa face-centered cubic (fcc) pattern, where small peaks from the double hexagonal close-packed (dhcp) structure are observed, and the 22.4 GPa α-U pattern, where small peaks from the body-centered orthorhombic (bco) structure are seen.

Material [28]. The onset pressure is defined as the first appearance of any reflections from the higher-pressure phase, and in some cases, not enough reflections are observed to obtain a volume for that phase at that pressure. All pressures that will be quoted below are determined from the Cu EOS reported by Ref. [29]. In this run, we observe Pr-II (fcc) at 5.2(5) GPa, Pr-III (d-fcc) at 9.2(5) GPa, Pr-VII (bco) at 13.5(1.2) GPa, and Pr-IV (α-U) at 20.9(4) GPa. The uncertainties associated with these transition pressures include the uncertainty in pressure determined from the Cu EOS (uncertainty in peak positions and uncertainty in fitted EOS parameters) which are small at these pressures. It also includes the pressure difference between the pattern where the high-pressure phase is first observed and the previous pattern where the pure low-pressure phase is observed. Additionally, the textured nature of the sample also introduces an uncertainty that is not easy to quantify due to observation bias caused by texturing of the sample. Note that our constraint on the onset pressure of the Pr-VII (bco) transition is limited since the previous data point was collected at 13.5 GPa. One subtle difference in the onset of the bco Pr-VII phase is that we do not observe the (006) reflection becoming more intense than the (202) reflection; it does, however, become broader, as previously reported [21]. We do

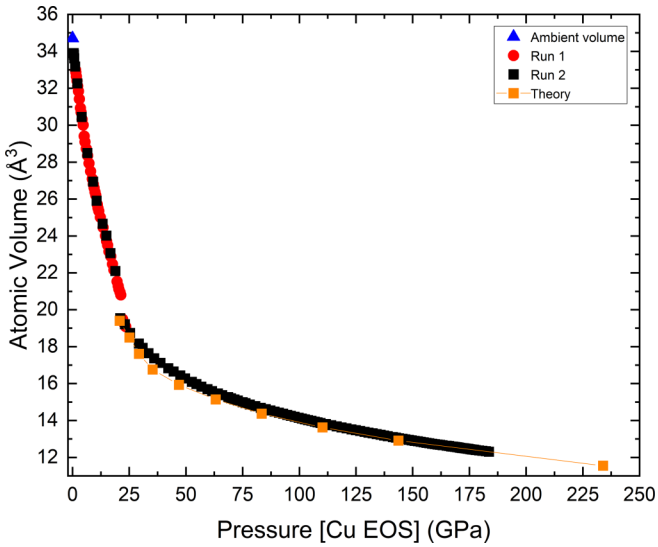

FIG. 2. Pressure-volume curve of Pr compressed in a Ne pressure-transmitting medium (PTM) up to 185 GPa. Ambient volume, run 1, run 2 and our density functional theory (DFT) + orbital polarization (OP) calculated results (for the α-U phase) are all shown. See Ref. [28] for comparison with previous studies [13,18–21].

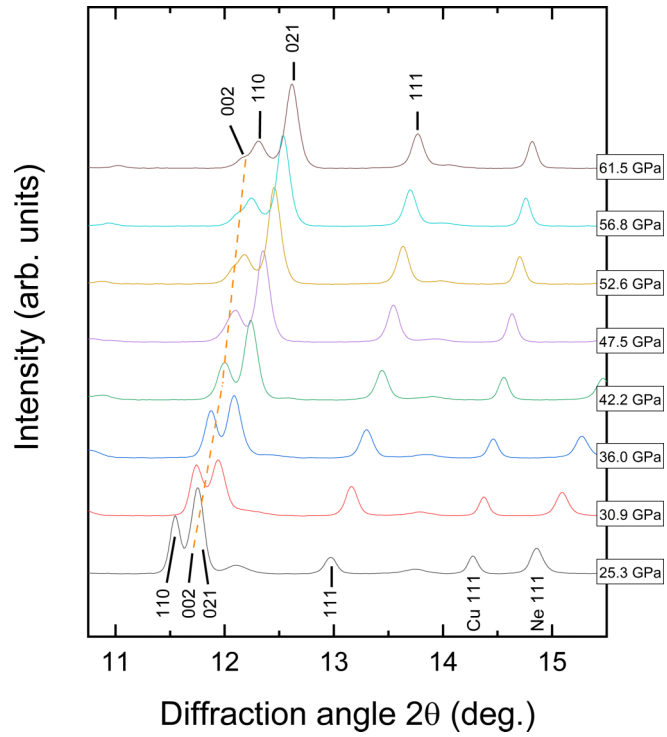

FIG. 3. Integrated diffraction patterns from run 2 showing the behavior of the positions of the (021), (002), and (110) reflections from ~25 to ~62 GPa. This is like what has been reported in U, where the (002) reflection shifts less than the (021) and (110) reflections, so that it moves to the low-angle side of the triplet under compression.

observe a reflection appearing between the (00,12) and (404) reflections consistent with what Evans *et al.* [21] reported. We do not observe the completion of the volume collapse phase transition in this run and observe coexistence of Pr-VII (bco) and Pr-IV (α-U) from 21.0 GPa to the maximum pressure of this run 23.5 GPa.

In run 2, we collected diffraction patterns up to a maximum pressure of 185 GPa in a Ne PTM. While we see the same structural sequence as in run 1, our pressure resolution was lower due to the higher targeted maximum pressure of this run. We observe the same cubic contaminant (fcc structure) as in run 1, but the reflections are even weaker than in run 1, and they are only observed in a few patterns in the stability field of Pr-II. Notably, we do not observe any reaction between Pr and Ne in either run.

In Fig. 2, we show the pressure-volume curve obtained from runs 1 and 2 and our DFT calculated volumes; for clarity, we did not plot our results with previous studies [13,18–21] (for comparison with previous studies see Ref. [28]). As discussed in Sec. II, we calculated the volumes of each phase of Pr directly from our fitted peak positions. For the phases before the volume collapse (Pr-I, Pr-II, Pr-III, and Pr-VII), there is no difference between the volumes calculated from our fitted reflections and the Rietveld refinements of the full diffraction pattern. We show the lattice parameters for the phases before the volume collapse obtained from our peak fit approach in Ref. [28]. For the α-U phase of Pr, there is a slight difference between the lattice parameters obtained from the Rietveld refinements and the lattice parameters calculated from the (110), (021), and (002) reflections (see Ref. [28]). The largest discrepancy is seen in the c axis in the ~20–50 GPa pressure range where the Rietveld refined volumes are at most 1.12% smaller than those calculated directly from the peak fitted reflections. From 50 to 185 GPa, the difference is <0.5%, while the difference for the a and b axes is at most 0.5% in the 20–50 GPa range and <0.15% different from 50–185 GPa (see Ref. [28]). The agreement between these two approaches is remarkable, and the slightly larger disagreement in the c axis is likely due to a bias introduced by calculating the c axis directly from the (002) reflection. The pressure shift of this reflection will be discussed in further detail below.

The response of α-U structured Pr to compression is like what has been reported in other α-U structured materials. The relative compressibilities of the lattice parameters of α-U structured Pr show that c is the least compressible followed by a and the b axis being most compressible. For α-U structured U, the c axis is also the least compressible, while the compressibility of the a and b axes is nearly identical. The reason for this high-pressure behavior of α-U has been argued to be related to electrostatic interactions [38]. For α-U structured Nd, the a axis is most compressible, with both the b and c axes being the least compressible. This anisotropic compression of α-U structured materials can be revealed when the pressure evolution of the triplet containing the (021), (002), and (110) reflections is investigated. Shown in Fig. 3, the (002) reflection is observed in the middle of the triplet and shifts relative to (021) and (110) to the low-angle side of the triplet under compression. These three peaks can be easily deconvolved across this pressure range, and by ~52 GPa, the (002) reflection can be easily distinguished visually. Similarly, in U, (002) starts on the high-angle side of the triplet at ambient conditions, and by 100 GPa, it is on the low-angle side of the triplet [22],

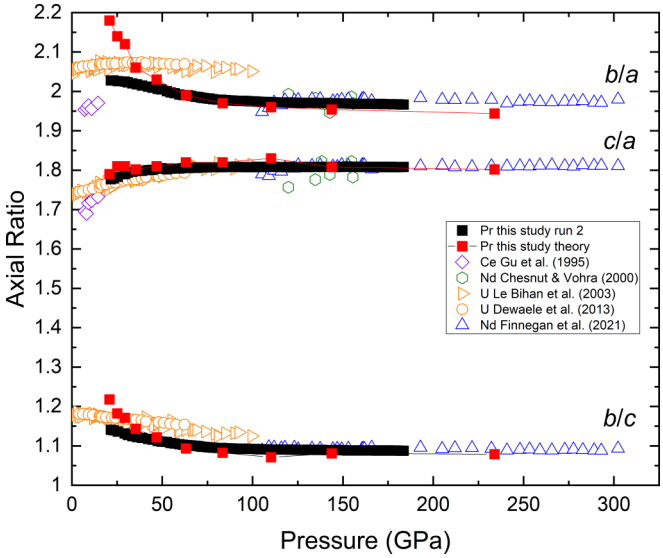

FIG. 4. Axial ratios of α-U structured Pr from run 2 and our density functional theory (DFT) calculations and Ce, Nd, and U from Refs. [8,24,25,39,40] as functions of pressure.

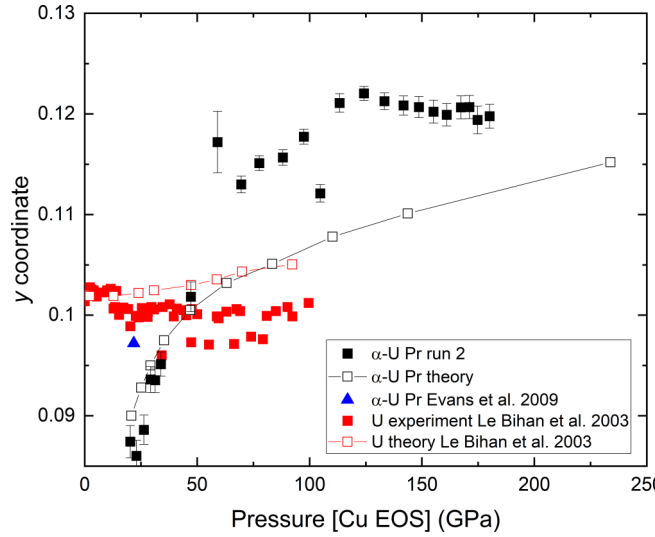

FIG. 5. Atomic positional parameter y for α-U structured Pr and U from Ref. [24] as a function of pressure. Relatively good agreement is seen in the refined values from run 2 and our density functional theory (DFT) calculated values. U shows very little change as a function of pressure, while theory predicts that it will increase as pressure increases.

whereas in Nd, the (002) reflection is on the low-angle side of the triplet when it transforms at ∼100 GPa and remains on the low-angle side up to 302 GPa [8]. The relative shift of the (002) reflection provides direct crystallographic evidence for the anisotropic compressibility, and it can be further understood when the topology of the α-U structure is considered.

Previous studies have not reported the lattice parameters of Pr across the entire pressure range of their measurements. We plotted the available lattice parameters from Refs. [21–23] and show them in Ref. [28]. There is good agreement between both run 1 and 2 from this paper and the previous studies. Our data provide a more detailed look at the pressure evolution of the lattice parameters across the entire structural transition sequence through the volume collapse up to 185 GPa. Further insight into the behavior of α-U structured Pr can be gained by looking at the axial ratios as a function of pressure. Figure 4 shows the axial ratios for Pr from run 2 and our DFT as well as α-U structured Ce, Nd, and U [25,39,40]. The axial ratios from our DFT calculations correctly capture the trend in each axial ratio but show larger values initially for both b/a and b/c. This is because theory initially overestimates the length of the b axis, while it underestimates the length of the a and c axes relative to our experimental values. Interestingly, for Pr and Nd, all three axial ratios converge on the same values >100 GPa. The reported c/a and b/c ratios of U appear to behave like Pr and Nd, while b/a shows a slightly different trend. For Ce, only the volumes and the axial ratios b/a and c/a were reported. Here, c/a in Ce increases as pressure increases, which is seen in Pr, Nd, and U, and b/a is relatively flat like U. However, the pressure range over which α-U structured Ce is stable is too narrow to establish a reliable trend for comparison with the trends seen in Pr, Nd, and U. For the α-U structure, the b/a ratio can provide information on the distortion of hexagonal close-packed (hcp) atomic layers; an ideal value is $\sqrt{3} = 1.732$. For Pr, the b/a ratio indicates that the hcp atomic layers become less distorted from ∼21 to 75 GPa. Above ∼75 GPa, it remains essentially constant, indicating no further changes in the distortion of the hcp layers occur across this pressure range.

As noted above, we performed Rietveld refinements at various pressures across the entire pressure range that we observed α-U structured Pr to be stable, and in these refinements, we also refined the positional parameter y. It should be noted that this parameter depends on peak intensities not peak positions. Thus, the textured nature of our patterns contributes to our uncertainties on the y coordinate. We show in Fig. 5 our refined positional parameter y from run 2 and our DFT calculated positional parameter y as a function of pressure. Both our experimentally derived values and the theoretically derived values show the same trend as a function of pressure. While there is reasonable agreement between experiment and theory, the scatter in our refined values is likely due to the textured nature of our diffraction patterns. The positional parameter y determined from both theory and experiment has also been reported for U [25], and it shows very little change as a function of pressure, which contrasts with Pr.

In run 2, α-U structured Pr is stable from the volume collapse at ∼20 GPa to the maximum pressure of this run which was 185 GPa. We do not see evidence for the transition to a primitive orthorhombic structure with the space group $P2_12_12_1$ proposed by Velisavljevic and Vohra [13]. In Fig. 6, we show Rietveld refinements at ∼97, 155, and 180 GPa. We do not observe a reflection growing in near the α-U (111) Pr reflection (see Ref. [28]), and all patterns collected from ∼20 to 185 GPa can be indexed to the α-U (*Cmcm*) structure. Additionally, the axial ratios shown in Fig. 4 do not show any discontinuities or changes in slope near the pressure of the proposed phase transition. We also performed Rietveld refinements at ∼157 GPa using both the α-U structure and the proposed $P2_12_12_1$ structure, and we found that the reflec-

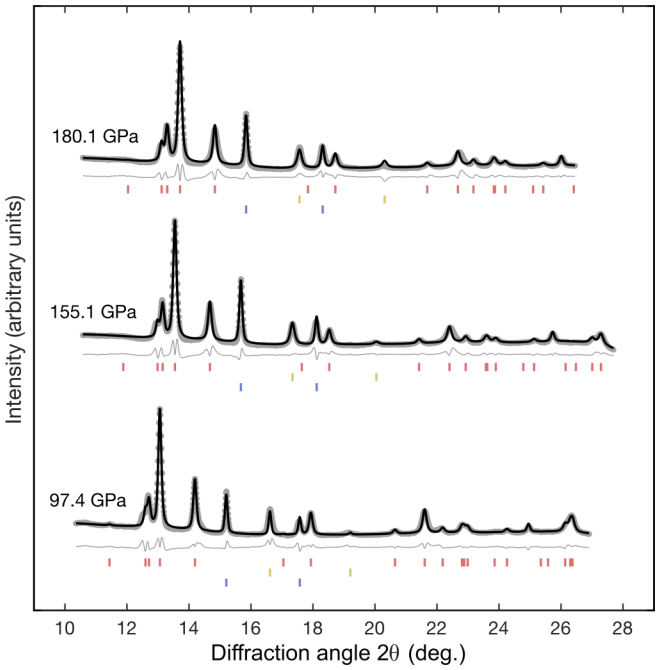

FIG. 6. Rietveld refinement results for data collected at three select pressures: 97.4, 155.1, and 180.1 GPa from run 2. The associated predicted reflections are plotted underneath their respective patterns for copper (blue), neon (yellow), and the Pr α-U phase (red).

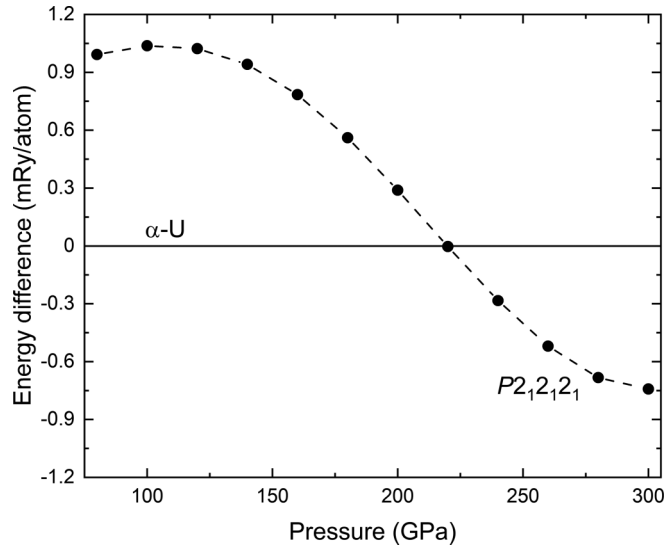

FIG. 7. Calculated (solid circles) energy difference between α-U Pr and $P2_12_12_1$ Pr (α-U Pr as the reference). Dashed line is guide to the eye only. Above ~220 GPa, the $P2_12_12_1$ Pr is stable over the α-U Pr. Note that, across the pressure range of our experimental results, the α-U of Pr is predicted to be the stable phase, in agreement with our measurements.

tions unique to the $P2_12_12_1$ structure are not observed in our diffraction pattern (see Ref. [28]). The R_{wp} of our Rietveld refinements is <4% for all our fits. There are various Rietveld discrepancy values (e.g., goodness of fit, χ^2, and R factors), and it is important to also determine the quality of the Rietveld fit by viewing the observed and calculated patterns graphically as well as ensuring that the structural model is chemically plausible [41].

We investigated the α-U phase as well as the proposed $P2_12_12_1$ phase using DFT + OP over a wide pressure range from ~80 up to ~300 GPa and found that the α-U phase is favored over the $P2_12_12_1$ phase up to at least 220 GPa. Hence, for the highest pressure measured, our experiments and theory agree; Pr is stable in the α-U phase. Above ~220 GPa, however, our DFT + OP model suggests the $P2_12_12_1$ phase may in fact form. However, we emphasize that a thorough search for other phases was not conducted. In Fig. 7, we show the energy difference between the α-U and $P2_12_12_1$ phases as a function of pressure. Here, the energy for the α-U phase is the reference. Notice that the energy for the $P2_12_12_1$ phase becomes lower than the α-U phase above ~220 GPa, suggesting an α-U-to-$P2_12_12_1$ phase transition.

As discussed in the introduction, nonhydrostatic stress can affect phase transitions such as lowering the onset pressure of a phase transition, stabilizing different crystalline phases, and even inducing amorphization [15]. The experiment of Velisavljevic and Vohra [13] did not use a PTM, which is the most likely explanation for why they see a distortion of the α-U at ~147 GPa. Additionally, they carried out electrical resistivity measurements which they use as further evidence for the proposed phase transition [12]. However, those measurements were also nonhydrostatic, so it is likely that they are observing the same distortion due to nonhydrostatic conditions. Further evidence that nonhydrostatic conditions influenced their results can be seen in their reported P-V curve which plots above our data [28] which were collected using a Ne PTM. Interestingly, as discussed above, our theoretical calculations predict that the $P2_12_12_1$ structure would become stable over the α-U structure above ~220 GPa. It is possible that nonhydrostatic conditions lowered the boundary of this transition by >70 GPa. However, we note that we did not consider other structures in our calculations, and there may be other structures that are lower in energy. We also evaluated our results for uniaxial stress using the line-shift approach [42–44], and we found that the uniaxial stress sustained by the Cu pressure marker increases to ~1.2 GPa at the maximum pressure of 185 GPa [28]. We also inspected our raw diffraction patterns by looking at the caked images, and the reflections from the sample appear as straight lines, indicating that the stress field in the high-pressure compartment is quite uniform [28].

Notably, we observe residual peaks which belong to Pr-VII (bco) up to ~38 GPa. Cunningham *et al.* [20] discuss the growth of the α-U phase in Pr and that mixed phase patterns are seen at 18.9 GPa. The next pattern they show at 40.4 GPa; they state that pure α-U phase is observed. Since they do not show patterns in between these two pressures, and it is not explicitly discussed in the text, it is unclear if they also observed mixed phase patterns between 18.9 and 40.4 GPa. Evans *et al.* [21] report that mixed-phase bco-Pr and α-U Pr patterns were observed between 20.5 and 21.8 GPa. We fit the Pr α-U P-V data from run 2 to a Vinet [45] EOS. The pressure range we used for our EOS fit was from 38 to 185 GPa, where pure α-U Pr is observed. There are not enough reflections observed from bco-Pr to obtain reliable volumes for this phase in the ~20–38 GPa pressure range. Our Vinet

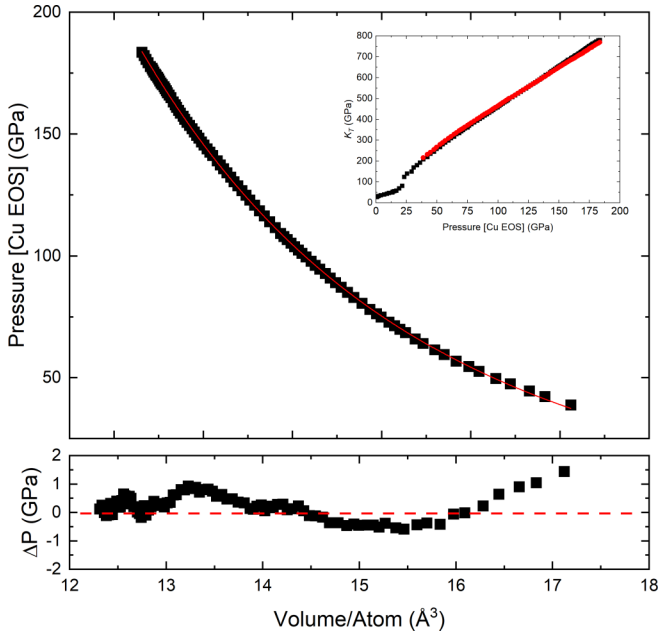

FIG. 8. Pressure-volume relationship of α-U Pr obtained from run 2; solid line shows our best fit Vinet equation of state (EOS). The difference between the data points and the Vinet EOS fit is presented in the lower panel. Inset shows the bulk modulus as a function of pressure calculated from the fitted EOS (red circles from 38 to 185 GPa) and as directly calculated from the *P*-*V* data (black squares).

fit parameters from the *P*-*V* data using Ne as our pressure calibrant are $V_0 = 23.75 \pm 0.26$ Å^3, $K_0 = 42 \pm 3.4$ GPa, and $K_0^{'} = 6.29 \pm 0.11$. When Cu is used to calibrate the pressure, the following parameters are obtained with $V_0 = 24.54 \pm 0.29$ Å^3, $K_0 = 33 \pm 2.8$ GPa, and $K_0^{'} = 6.60 \pm 0.11$. Figure 8 shows our best fitting Vinet EOS to the *P*-*V* data from run 2 using Cu as our pressure calibrant as well as the difference between the data points and the Vinet EOS fit. The inset shows the bulk modulus of Pr as a function of pressure; we calculated the isothermal bulk modulus from our fitted EOS parameters and directly from our *P*-*V* data using $K_T = -V(\partial P/\partial V)$. The second approach does not rely on assumptions that are used in the derivation of the chosen EOS. The slope of the bulk modulus as a function of pressure is slightly different between the two different methods. At the maximum pressure, the bulk modulus calculated from our EOS fit is 1.5% lower than the bulk modulus calculated directly from the *P*-*V* data. The bulk modulus of Pr increases as pressure increases with a discontinuous shift to higher values across the volume collapse transition (bco to α-U). This contrasts with Ce, where the bulk modulus decreases in the γ-Ce phase until it reaches the volume collapse transition, where it starts increasing again in the α-Ce phase [46,47].

IV. CONCLUSIONS

We compressed praseodymium metal in a soft PTM up to a maximum pressure of 185 GPa. We observe the previously reported high-pressure structural transition sequence where Pr-II (fcc) is observed at 5.2 GPa, Pr-III (d-fcc) at 9.2 GPa, Pr-VII (bco) at 13.5 GPa, and Pr-IV (α-U) at 20.9 GPa. Additionally, we observe the coexistence of bco-Pr and α-U Pr from ~20 up to ~38 GPa. The α-uranium structure of Pr is stable from 20 to 185 GPa, and no evidence of the proposed transition to a primitive orthorhombic structure >147 GPa was observed. This may be due to the nonhydrostatic conditions in the previous studies [12,13] either stabilizing a primitive orthorhombic phase or lowering the onset pressure of the transition to a primitive orthorhombic phase. Additionally, we found that the lattice parameters obtained from simple peak fitting and those obtained from Rietveld refinements of the full diffraction patterns show remarkably good agreement. This is not fortuitous but rather the result of careful sample/DAC preparation and the use of a soft PTM. Since we do not observe any reaction between Pr and Ne in this paper, it is likely Ne would not react with other lanthanides at high pressure. We calculated the lattice parameters and *y* coordinate for α-U Pr and found good agreement between our calculations and experimental measurements. We find that the bulk modulus of Pr increases with increasing pressure and that there is a discontinuous increase across the volume collapse transition. For the α-U phase of Pr, we find a good agreement between the bulk modulus as calculated directly from the *P*-*V* data and the bulk modulus calculated using the fitted EOS parameters. The calculated energies of the proposed primitive orthorhombic structure and the α-U structure at ~150 GPa show that the α-U structure is lower in energy and that the $P2_12_12_1$ structure may become stable >220 GPa.

ACKNOWLEDGMENTS

We thank S. Finnegan and M. McMahon for providing the lattice parameters for α-U structured Nd from their recent publication (Ref. [8]). E.F.O. thanks I. Cube for helpful discussions. This paper was performed under the auspices of the U.S. Department of Energy (DOE) by Lawrence Livermore National Laboratory under Contract No. DE-AC52-07NA27344. O.S.P. acknowledges the support of DOE National Nuclear Security Administration (NNSA) Stewardship Science Graduate Fellowship (DE-NA0003960). Portions of this paper were performed at HPCAT (Sector 16), Advanced Photon Source (APS), Argonne National Laboratory. HPCAT operations are supported by DOE-NNSA's Office of Experimental Sciences. The APS is a DOE Office of Science User Facility operated for the DOE Office of Science by Argonne National Laboratory under Contract No. DE-AC02-06CH11357.

[1] M. I. McMahon, S. Finnegan, R. J. Husband, K. A. Munro, E. Plekhanov, N. Bonini, C. Weber, M. Hanfland, U. Schwarz, and S. G. Macleod, Phys. Rev. B **100**, 024107 (2019).

[2] U. Benedict, W. A. Grosshans, and W. B. Holzapfel, Physica B+C **144**, 14 (1986).

[3] K. A. Gschneidner, J. Alloys Compd. **223**, 165 (1995).

[4] W. B. Holzapfel, Physica B **190**, 21 (1993).
[5] W. B. Holzapfel, J. Alloys Compd. **223**, 170 (1995).
[6] B. Johansson, Hyperfine Interact. **128**, 41 (2000).
[7] S. E. Finnegan, E. J. Pace, C. V. Storm, M. I. McMahon, S. G. MacLeod, H. P. Liermann, and K. Glazyrin, Phys. Rev. B **101**, 174109 (2020).
[8] S. E. Finnegan, C. V. Storm, E. J. Pace, M. I. McMahon, S. G. MacLeod, E. Plekhanov, N. Bonini, and C. Weber, Phys. Rev. B **103**, 134117 (2021).
[9] C. S. Perreault and Y. K. Vohra, High Pressure Res. **40**, 392 (2020).
[10] Q. C. Li, H. Ehteshami, K. Munro, M. Marques, M. I. McMahon, S. G. MacLeod, and G. J. Ackland, Phys. Rev. B **104**, 144108 (2021).
[11] Y. K. Vohra, S. L. Beaver, J. Akella, C. A. Ruddle, and S. T. Weir, J. Appl. Phys. **85**, 2451 (1999).
[12] N. Velisavljevic, K. M. MacMinn, Y. K. Vohra, and S. T. Weir, Appl. Phys. Lett. **84**, 927 (2004).
[13] N. Velisavljevic and Y. K. Vohra, High Pressure Res. **24**, 295 (2004).
[14] G. K. Samudrala, S. A. Thomas, J. M. Montgomery, and Y. K. Vohra, J. Phys.: Condens. Matter **23**, 315701 (2011).
[15] K. Takemura, High Pressure Res. **41**, 155 (2021).
[16] K. Takemura, J. Phys. Soc. Jpn. **76**, 202 (2007).
[17] A. Dewaele and P. Loubeyre, High Pressure Res. **27**, 419 (2007).
[18] B. J. Baer, H. Cynn, V. Iota, C. S. Yoo, and G. Y. Shen, Phys. Rev. B **67**, 134115 (2003).
[19] G. N. Chesnut and Y. K. Vohra, Phys. Rev. B **62**, 2965 (2000).
[20] N. C. Cunningham, N. Velisavljevic, and Y. K. Vohra, Phys. Rev. B **71**, 012108 (2005).
[21] S. R. Evans, I. Loa, L. F. Lundegaard, and M. I. McMahon, Phys. Rev. B **80**, 134105 (2009).
[22] H. K. Mao, R. M. Hazen, P. M. Bell, and J. Wittig, J. Appl. Phys. **52**, 4572 (1981).
[23] W. A. Grosshans, Y. K. Vohra, and W. B. Holzapfel, J Phys. F: Met. Phys. **13**, L147 (1983).
[24] T. Le Bihan, S. Heathman, M. Idiri, G. H. Lander, J. M. Wills, A. C. Lawson, and A. Lindbaum, Phys. Rev. B **67**, 134102 (2003).
[25] A. Dewaele, J. Bouchet, F. Occelli, M. Hanfland, and G. Garbarino, Phys. Rev. B **88**, 134202 (2013).
[26] P. Söderlind, Phys. Rev. B **65**, 115105 (2002).
[27] Zs. Jenei, H. Cynn, K. Visbeck, and W. J. Evans, Rev. Sci. Instrum. **84**, 095114 (2013).
[28] See Supplemental Material at http://link.aps.org/supplemental/10.1103/PhysRevB.105.144107 for details associated with the ambient structure refinement, characterization of cubic contaminant, comparison to previous datasets, high-pressure structure refinements, characterization of the stress state in the DAC, and tables of experimental and calculated data.
[29] A. Dewaele, P. Loubeyre, and M. Mezouar, Phys. Rev. B **70**, 094112 (2004).
[30] A. Dewaele, F. Datchi, P. Loubeyre, and M. Mezouar, Phys. Rev. B **77**, 094106 (2008).
[31] A. Dewaele, M. Torrent, P. Loubeyre, and M. Mezouar, Phys. Rev. B **78**, 104102 (2008).
[32] J. S. Smith, E. A. Rod, and G. Shen, Rev. Sci. Instrum. **90**, 015116 (2019).
[33] C. Prescher and V. B. Prakapenka, High Pressure Res. **35**, 223 (2015).
[34] B. H. Toby and R. B. Von Dreele, J. Appl. Crystallogr. **46**, 544 (2013).
[35] P. Söderlind, P. E. A. Turchi, A. Landa, and V. Lordi, J. Phys.: Condens. Matter **26**, 416001 (2014).
[36] J. M. Wills, M. Alouani, P. Andersson, A. Delin, O. Eriksson, and O. Grechnyev, in *Full-Potential Electronic Structure Method;* Springer Series in Solid-State Sciences (Springer, Berlin, Heidelberg, 2010), Vol. 167.
[37] J. P. Perdew, Physica B **172**, 1 (1991).
[38] J. Akella, S. Weir, J. M. Wills, and P. Söderlind, J. Phys.: Condens. Matter **9**, L549 (1997).
[39] G. L. Gu, Y. K. Vohra, and K. E. Brister, Phys. Rev. B **52**, 9107 (1995).
[40] G. N. Chesnut and Y. K. Vohra, Phys. Rev. B **61**, R3768 (2000).
[41] B. H. Toby, Powder Diffr. **21**, 67 (2006).
[42] A. K. Singh, J. Appl. Phys. **73**, 4278 (1993).
[43] A. K. Singh, C. Balasingh, H. K. Mao, R. J. Hemley, and J. F. Shu, J. Appl. Phys. **83**, 7567 (1998).
[44] K. Takemura and A. Dewaele, Phys. Rev. B **78**, 104119 (2008).
[45] P. Vinet, J. Ferrante, J. R. Smith, and J. H. Rose, J. Phys. C: Solid State Phys. **19**, L467 (1986).
[46] M. J. Lipp, D. Jackson, H. Cynn, C. Aracne, W. J. Evans, and A. K. McMahan, Phys. Rev. Lett. **101**, 165703 (2008).
[47] M. J. Lipp, Zs. Jenei, H. Cynn, Y. Kono, C. Park, C. Kenney-Benson, and W. J. Evans, Nat. Commun. **8**, 1198 (2017).